Med Biol Eng Comput (2013) 51:1091–1104
DOI 10.1007/s11517-013-1089-7

ORIGINAL ARTICLE

Automatic segmentation of brain MR images using an adaptive balloon snake model with fuzzy classification

Hung-Ting Liu · Tony W. H. Sheu · Herng-Hua Chang

Received: 10 December 2012 / Accepted: 25 May 2013 / Published online: 7 June 2013

Abstract Skull-stripping in magnetic resonance (MR) images is one of the most important preprocessing steps in medical image analysis. We propose a hybrid skull-stripping algorithm based on an adaptive balloon snake (ABS) model. The proposed framework consists of two phases: first, the fuzzy possibilistic c-means (FPCM) is used for pixel clustering, which provides a labeled image associated with a clean and clear brain boundary. At the second stage, a contour is initialized outside the brain surface based on the FPCM result and evolves under the guidance of an adaptive balloon snake model. The model is designed to drive the contour in the inward normal direction to capture the brain boundary. The entire volume is segmented from the center slice toward both ends slice by slice. Our ABS algorithm was applied to numerous brain MR image data sets and compared with several state-of-the-art methods. Four similarity metrics were used to evaluate the performance of the proposed technique. Experimental results indicated that our method produced accurate segmentation results with higher conformity scores. The effectiveness of the ABS algorithm makes it a promising and potential tool in a wide variety of skull-stripping applications and studies.

H.-T. Liu · H.-H. Chang (✉)
Computational Biomedical Engineering Laboratory (CBEL), Department of Engineering Science and Ocean Engineering, National Taiwan University, 1, Sec. 4, Roosevelt Road, Daan, 10617 Taipei, Taiwan
e-mail: herbertchang@ntu.edu.tw

T. W. H. Sheu
Department of Engineering Science and Ocean Engineering, National Taiwan University, 1, Sec. 4, Roosevelt Road, Daan, 10617 Taipei, Taiwan

Keywords Skull-stripping · Segmentation · Active contours · Fuzzy possibilistic c-means · MRI

1 Introduction

Medical imaging is essential and important to biomedical research and clinical applications due to its valuable intravital information. Among various medical image modalities, magnetic resonance imaging (MRI) provides high contrast images that has been widely used in the interpretation and visualization of various anatomical structures. Segmentation in MR images plays a fundamental role and simplifies subsequent analysis procedures by extracting certain useful anatomical structures. Intuitively, the segmentation work is carried out by experts such as doctors and physicians. However, as the amount of MR image data is exploding nowadays, manual segmentation has the following disadvantages [33]:

(1) Due to the complex anatomical structure in MR images, the slice-by-slice manual segmentation is time-consuming and tedious.
(2) The identification of target boundary is subjective and the segmentation results with user-intervention is prone to operator bias.
(3) The nonreproductivity of manual segmentation is less effective and impractical to the huge amount of MR image data.

Consequently, a wide variety of studies have been devoted on semi- or fully automatic computer-aided segmentation for achieving fast and objective segmentation with high accuracy to facilitate subsequent analyses. In particular, skull-stripping, belonging to one of the preprocessing step in medical image analysis, aims to remove the

non brain tissues and leave the entire brain region. In essence, the white matter (WM), gray matter (GM), and cerebrospinal fluid (CSF) compose the three major components of the brain region. Many existing skull-stripping methods are devoted on the extraction of the cerebrum and cerebellum while the identification of the brain stem varies subject to specific applications. In addition to skull-stripping methods, numerous contributions have been made on the individual segmentation of the GM, WM, and CSF [17, 38] as well as the corpus callosum, ventricles, hippocampus, and caudate nuclei [24].

In general, research carried out in the field of skull-stripping can be broadly classified into three categories. The first category consists of a series of morphological operators along with statistical analysis. Wang and Fu [39] presented the definition of basic operations. Stokking et al. [31] suggested an automatic model based on histogram and thresholding followed by morphological operations. Chiverton et al. [6] proposed a fully automatic skull stripper experimented on both adult and infant subjects. Shattuck et al. [27] developed the brain surface extractor (BSE), which combines a series of low-level skull-stripping operations followed by image nonuniformity compensation to extract the brain surface in T1-weighted MR images.

In the BSE model, the anisotropic diffusion filter is first used to smooth noisy regions while preserving salient edges. The diffusion coefficient is designed to adaptively control the diffusion size using the image intensity gradient for edge length estimation. The Marr-Hildreth edge detector is then used to locate the boundary of the brain surface by a symmetric Gaussian filter followed by the Laplacian filter. This detector is known for its low computational cost and results in a closed contour, which is superior to other edge detection filters such as Canny, Sobel, and Deriche. After the filtered image volume I_c is obtained, the 1-value voxels, which constitutes the non edge region, are computed and denoted as $F = \{f_k : I_c(k) = 1\}$. Lastly, the morphological operations are applied to isolate the brain tissue from the original image volume using the information provided by F. The closing operation is further adopted to fill the holes within the brain region.

The second category is based on classification and clustering algorithms that categorize each voxel according to the intensity and local patterns. The support vector machine (SVM) [32, 34] is one of the representative statistical classifiers beside the typical tools such as Bayesian, neural networks, and nearest neighbor methods. The SVM model marks voxels as belonging to a unique class by determining a set of hyperplanes that maximizes the separation between classes [13, 34]. For more details on the SVM, please refer to the review paper [28]. On the other hand, much attention has been devoted to the classifiers based on K-means algorithms such as fuzzy c-means (FCM), which is the enhanced version of c-means [2] and possibilistic c-means (PCM) [15]. A hybridization of the above two models, known as fuzzy possibilistic c-means (FPCM), was developed to exploit the advantages of these two methods [20, 21].

The third category is based on active contour models (ACMs) that deform the contour to fit salient edges in images. Among several types of ACMs, snakes, proposed by Kass et al. [14], are a parametric model that deforms contours under the guidance of geometric properties and local image information based on the energy-minimization concept. However, snake-based methods suffer from the following problems:

(1) Moving distance limitation: a contour segment locating at the homogeneous region is guided only by forces based on its geometric properties. Consequently, the moving distance is limited and has difficulties of evolving into concavities.
(2) Multiple object segmentation: the basic nature of the snake model is designed for single object segmentation. The abilities of splitting and merging during convergence are not straightforward and easy using snakes.

To address these problems, Cohen [7, 8] proposed an enhanced version with a balloon force that drives the contour moving toward the normal direction. Phumeechanya et al. [23] suggested a framework using extensible search lines to detect the forward and backward regions of each contour points in an attempt to decide the moving direction. Aside from the balloon snake embedding forces on the contour points, Xu and Prince [41] proposed the gradient vector flow (GVF) snake, which diffuses the edge map derived from the image. The gradient vector provides the enhanced external force field that enlarges the capture range. Wang et al. [40] developed the normally biased GVF (NBGVF) snake model that sets the diffusion and bias along the tangential and normal directions, respectively. The biasing weight is increased in homogeneous region while declined at boundaries. Alternatively, Tong et al. [37] suggested a criterion for the presence of multiple objects when the contour intersects itself. Li et al. [16] introduced segmentation on the external force field, and each segmented region is taken as a unique initialization of contours. Charfi [5] proposed the concept of using divergent points, which are generally located at homogeneous regions such as the inner part of an object and the gap between objects, thus providing meaningful information for snake splitting.

Of particular, the brain extraction tool (BET) [30] is one of the remarkable skull-stripping models that are based on deformable models associated with locally adaptive forces to fit the brain surface. The brain is modeled by a spherical

tessellated surface centered at the estimated center of gravity. Each vertex in the surface is moving under the guidance of an adaptive vector function, which is designed for driving the vertex in question to the mean position of its neighboring vertices. The first term in this equation is used for keeping all vertices in the surface equally spaced. For the second term, it acts to move the current vertex into lines with its neighboring vertices and hence increases the smoothness of the surface. Unlike the preceding terms involving smoothness, the third component drives the surface toward the expecting boundary. Finally, the sum of these three terms in each vertex determines the moving direction and distance.

Besides the described methods, there are abundant hybrid approaches for intracranial segmentation. For example, Shi et al. [29] proposed a level-set based learning (LSL) algorithm for brain extraction. A level-set- based fusion method was developed to combine multiple brain extractions associated with a closed smooth surface and the parameters were effectively learned from training data. Region growing based methods [22] connected regions based on predefined seeded regions along with histogram analysis, intensity thresholding, and morphological operations. Watershed techniques constitute a special instance of region-based methods with the gradient intensity used for defining connectivity. However, they are sensitive to noise and can often cause over-segmentation problems. To overcome this, a hybrid algorithm based on the combination of watershed algorithms and deformable surface models has been introduced [26]. The watershed algorithm was first applied to build an initial estimate of the brain volume followed by a surface deformation process to allow the incorporation of geometric constraints into the segmentation procedure. Another watershed-based skull stripping (WSS) algorithm [12] that combines the histogram characteristics and watershed techniques was also proposed. The WSS method first estimated tissue boundaries by finding inflection points in the image histogram. A watershed algorithm was then applied to fill the compartments defined from these boundaries, resulting in a skull stripped brain.

Several studies have shown that none of existing methods is able to process large-scale MR image data nowadays [3, 10]. Indeed, the combination of methods in different categories is necessary for achieving higher accuracy of skull-stripped results. Motivated by the effectiveness of deformable models and classifiers, this paper presents a new framework that combines the FPCM model with an adaptive balloon snake (ABS) model in an attempt to establish a more robust algorithm. The FPCM is used for classifying the brain image into five distinct classes, of which partially represents the CSF is used to enhance the image. The snake contour is then initialized outside the enhanced brain surface and shrunk to capture the brain region under the guidance of an adaptive balloon force. To evaluate the proposed ABS algorithm, several T1-weighted MR image data sets were segmented in comparison with existing state-of-the-art methods.

2 Methods

As illustrated in Fig. 1, the proposed algorithm consists of two major phases: image preprocessing and image segmentation.

2.1 Image preprocessing

The image preprocessing phase includes the preceding two blocks of the flow chart. First, input MR images are enhanced by a series of low level operations: pixels with

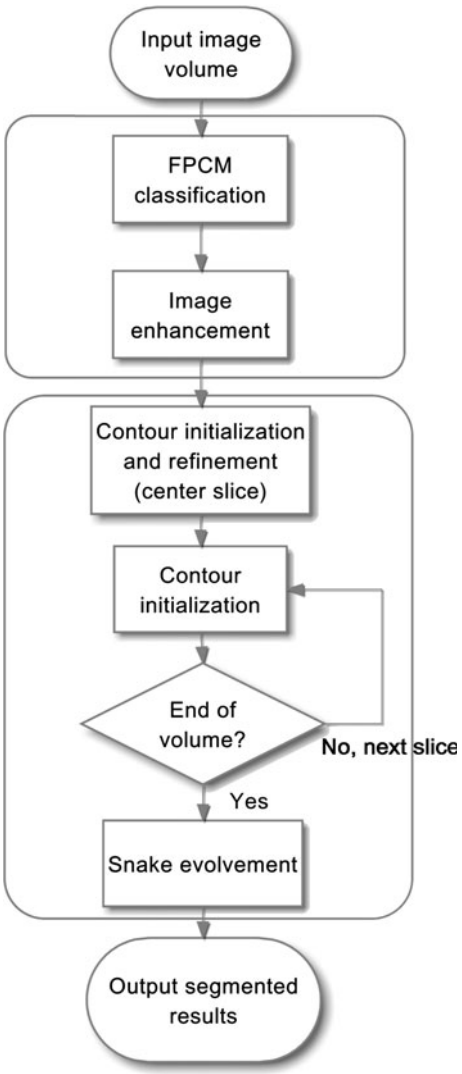

Fig. 1 Flowchart of the proposed skull-stripping algorithm

relatively high intensity values lying above 95 % of the cumulative histogram are treated as background and set to 0. The processed images are rescaled to an 8-bit intensity range [0, 255] using:

$$I'(x,y) = 255 \times \frac{I(x,y) - I_{\min}}{I_{\max} - I_{\min}}, \tag{1}$$

where $I(x, y)$ is the input image intensity located at (x, y), $I_{\max}$ and $I_{\min}$ are the maximum and minimum intensity values of I, respectively. To handle the random noise commonly existed in MR images, the scaled images are further smoothed by the bilateral filter [36], which is an edge-preserving operator that smoothes images while maintaining salient edges as given in the following equation.

$$\tilde{I}(x_0,y_0) = \frac{1}{C}\sum_{k=1}^{n} c_1 c_2 I'(x_k,y_k), \tag{2}$$

where

$$c_1 = \exp\left(\frac{-\|(x_k - x_0, y_k - y_0)\|^2}{2\sigma_d^2}\right) \tag{3}$$

and

$$c_2 = \exp\left(\frac{-|I'(x_k,y_k) - I'(x_0,y_0)|^2}{2\sigma_r^2}\right). \tag{4}$$

In Eq. (2), (x_k, y_k) represents the neighboring pixels located in the current window centered at (x_0, y_0) and n is the number of pixels in the corresponding window. The symbol $C = \sum_{k=1}^{n} c_1 c_2$ is used for intensity normalization. The FPCM algorithm is then applied to classify each slice into five clusters, and pixels in the same cluster are with an identical label as presented in Table 1. Detailed description of the FPCM algorithm is summarized in Appendix " 1".

Those classes in Table 1 are sorted and classified based on the mean intensity in each class. Specifically, class A mainly represents the image background and class B estimates the CSF and partial GM. Obviously, the mean intensity of class A is the lowest, while the mean intensity of class E is the highest. Subsequently, a series of morphological operations are carried out for enhancement as described below:

(1) Pixels belonging to class A or B are extracted from the classified image $\tilde{I}_{\text{fpcm}}$ and denoted as R_{ab} (the black region in Fig. 2c). The remaining classes in the image are treated as one region and denoted as R_{cde} (the white region in Fig. 2c).

(2) To make the region representing the CSF more salient, region R_{ab} is dilated by a structure element $se1$ (disk of radius 3):

$$R_{ab} \oplus \text{se1} = \{c \in \tilde{I}_{\text{fpcm}} \mid c = a + b, \text{ for some } a \in R_{ab} \text{ and } b \in \text{se1}\} \tag{5}$$

Region R_{ab} is accordingly expanded while R_{cde} is contrarily shrunk as shown in Fig. 2d.

(3) Since the brain surface is usually the largest connected component in the image [26, 27], other connected components in R_{cde} are removed. Besides, the holes inside R_{cde} are filled to make the region more compact as shown in Fig. 2e.

(4) In step 2, the brain region is slightly truncated owing to morphological dilation. To recover the missing part, dilation is applied again but on R_{cde} as shown in Fig. 2f using

$$R_{cde} \oplus \text{se1} = \{c \in \tilde{I}_{\text{fpcm}} \mid c = a + b, \text{ for some } a \in R_{cde} \text{ and } b \in \text{se1}\}. \tag{6}$$

(5) Region R_{cde} is further modified by morphological closing to maintain smoothness at the brain boundary. This step can significantly facilitate contour initialization for brain boundaries with severe concavities and convexities. The closing operation is described as follows:

$$R_{cde} \cdot \text{se2} = (R_{cde} \oplus \text{se2}) \ominus \text{se2}, \tag{7}$$

where closing is the combination of dilation followed by erosion with structure element se2 (disk of radius 5). For clarity, the processed R_{ab} and R_{cde} are denoted as R'_{ab} and R'_{cde}, respectively, as depicted in Fig. 2g.

(6) Finally, region R'_{ab} is superimposed on the filtered image $\tilde{I}$, i.e., pixels in $\tilde{I}$ corresponding to the pixels belonging to R'_{ab} in $\tilde{I}_{\text{fpcm}}$ are set to zero:

$$\tilde{I}_{\text{enh}}(x,y) = \begin{cases} 0, & \text{if} \tilde{I}_{\text{fpcm}}(x,y) \in R'_{ab} \\ \tilde{I}(x,y), & \text{otherwise} \end{cases}, \tag{8}$$

where $\tilde{I}_{\text{enh}}$ denotes the partially enhanced image. As shown in Fig. 2h, the processed image provides a somewhat clean and clear brain boundary for subsequent processing.

Table 1 Five classes and labels used in the FPCM classification algorithm

Class	Classification	Label
A	Background	1
B	CSF/GM	2
C	GM	3
D	WM/GM	4
E	WM	5

Morphological operations manipulated on the subsequent slices are more straightforward comparing to the center slice. Region R_{ab} obtained from the FPCM image is expanded by dilation. Subsequently, closing is proceeded on the largest connected component in region R_{cde} to generate a clear brain boundary.

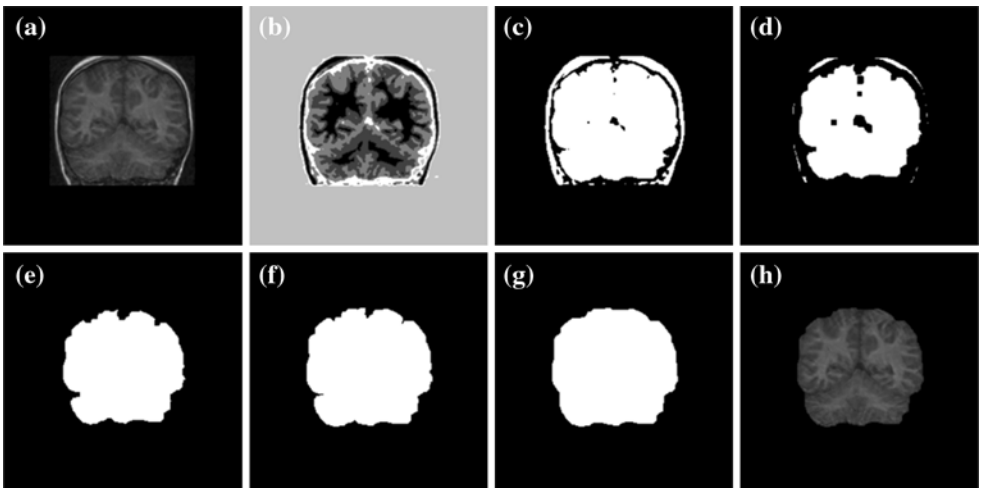

Fig. 2 Illustration of morphological operations for image enhancement. **a** Original image. **b** FPCM results. **c** R_{ab} and R_{cde}. **d** $R_{ab} \oplus$ se1. **e** The largest connected component with *holes filled*. **f** $R_{cde} \oplus$ se1. **g** $R_{cde} \bullet$ se2. The *black region* and the *white region* represent R'_{ab} and R'_{cde}, respectively. **h** $\tilde{I}_{\text{enh}}$

2.2 Image segmentation

The segmentation steps are summarized in the following four middle blocks in Fig. 1. While many existing methods place initial contours inside the brain [30, 35], we initialize the snake contour outside the brain surface after $\tilde{I}_{\text{enh}}$ is obtained.

2.2.1 Contour initialization on the center slice

Our segmentation starts from the center slice and continues on the subsequent slices until the whole volume is processed. In the center slice i, the initial snaxels $v_i = \{v_{i1}, v_{i2}, \ldots, v_{in}\}$ are successively generated clockwise by a sequence of searching paths, where n is the number of paths. The searching paths $p_i = \{p_{i1}, p_{i2}, \ldots, p_{in}\}$ are a set of lines generated clockwise on the center slice that record the pixel intensity values starting from the centroid C_i to the image border. Fig. 3a shows the brief view of contour initialization and notations. Detailed steps are described below:

(1) First, the centroid C_i of the searching paths is calculated using the geometric centroid of R'_{cde}, which is used for the starting searching point in each path.
(2) There exists one or more 0-intensity fragments in each searching path p_{ij}, one of which approximately represents the CSF position. Case 1: For searching paths with only one 0-intensity fragment, the snaxel v_{ij} is initialized at t_1 distance from the beginning of this detected fragment (t_1 equal to 5 pixels). Case 2: For two or more 0-intensity fragments on the searching path, the longest fragment (excluding the fragment from the skin to the image border) is considered to estimate the CSF position. The snaxel is initialized at t_2 percent from the beginning of this fragment (t_2 equal to 70). These two different scenarios with the case number indicated beside the corresponding searching path are illustrated in the right diagram of Fig. 3a.
(3) Repeat step 2 to obtain all initial snaxels clockwise path by path.

2.2.2 Contour refinement

After the initialization of snaxels surrounding the brain surface, refinement is applied to adjust the outlier positions that are poorly estimated. We do this by computing the distance from the centroid C_i to the estimated snaxel, which is denoted as $d_i = \{d_{i1}, d_{i2}, \ldots, d_{in}\}$, where $d_{ik} = |v_{ik} - C_i|$. The simple moving average (SMA) filter [9] is then used to measure the average of a subset in d_i:

$$\overline{d_{ik}} = \frac{1}{2h+1} \sum_{j=k-h}^{k+h} d_{ij} = \frac{1}{2h+1} \sum_{j=k-h}^{k+h} |v_{ij} - C_i|, \tag{9}$$

where $2h + 1$ is the number of snaxels included in the computation and $h = 5$. The difference between d_{ik} and $\overline{d_{ik}}$ is calculated and a snaxel v_{ik} is identified as an outlier if $|d_{ik} - \overline{d_{ik}}| > t$, where t is a prescribed threshold equal to 10. Finally, the snaxel outliers are replaced by the geometric centroid of adjacent snaxels as illustrated in Fig. 3b. It is evident that the contour becomes smoother after the refinement process and simultaneously maintains a nice shape corresponding to the brain surface.

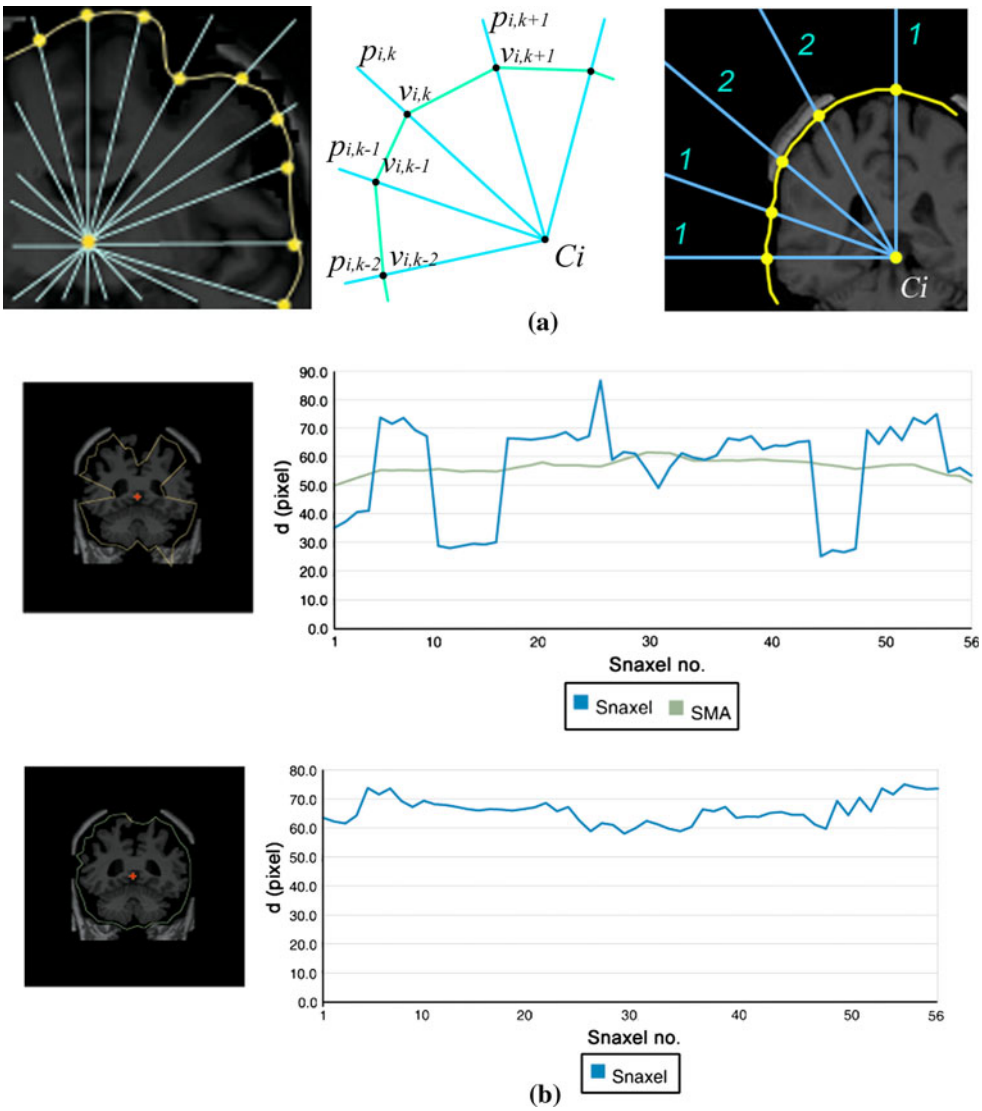

Fig. 3 **a** Illustration of contour initialization. *Left*; *Brief view* of initialized snaxels and searching paths. *Middle*: notations. *Right*: two cases of the searching paths. **b** Illustration of refinement process. *Top*: the estimated contour. The *blue line* represents the distances d_i from the snaxel v_i to the centroid C_i and the *green line* exhibits the corresponding distance $\overline{d_i}$ using the SMA filter. *Bottom*: the refined contour

2.2.3 Contour initialization on subsequent slices

Given the continuity of adjacent slices, snake contours on the processed neighboring slices can be used as a reference for the contour initialization of the current slice. Snaxels on the same searching path but locating at neighboring slices should have approximately close 2D spatial locations. For example, snaxels $v_{i,j}$ and $v_{i-1,j}$, locating at the jth searching path belonging to the $i-1$th and ith slices, respectively, might have nearly identical locations in 2D view. A narrow band centered at v_{i-1} is created on the ith slice for generating v_i. The narrow band is bounded on both sides of v_{i-1} with a bandwidth of 2δ as shown in Fig. 4a. In our approach, the snaxels v_i are located at the center of the fragment that is nearest to snaxels $v_{i-1,j}$ as illustrated in Fig. 4b, where the red dots represent snaxels $v_{i-1,j}$, the yellow dots denote the fragment centers, and the selected centers, i.e., snaxels $v_{i,j}$, are connected with dashed lines. Moreover, the estimated snaxel $v_{i,j}$ is replaced with the geometric centroid of $v_{i-1,j}$ and the selected fragment center if it is not in the narrow band. Two examples of using this strategy to obtain the initial contour are given in Fig. 4c, d.

2.2.4 Adaptive balloon force

Once all initial contours are computed, a balloon snake model is used for contour evolvement to obtain final skull-stripping results. As described in "Appendix 2", a traditional balloon snake model [7, 8] is formulated as internal, external, and balloon forces using $E_{\text{snake}} = \int_0^1 E_{\text{int}}(v(s)) + E_{\text{ext}}(v(s)) + E_{\text{bal}}(v(s))ds$, where $E_{\text{int}} = \alpha(s)|v_s|^2 + \beta(s)|v_{ss}|^2$ shortens the distances between adjacent snaxels, and the

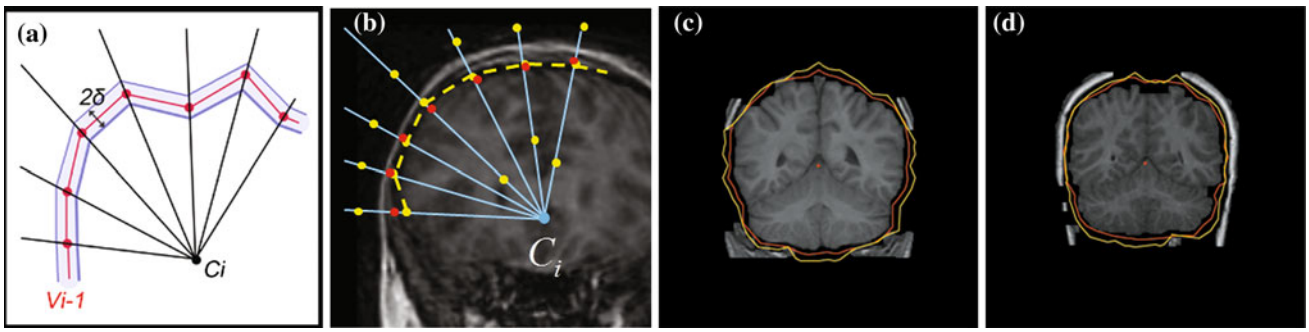

Fig. 4 Contour initialization on the subsequent slices. **a** Narrow band with a bandwidth 2δ. **b** The fragment centers on the $i-1$th slice and the estimated snaxels on the ith slice. **c** and **d** Two examples with complete initial contours

second order term makes the contour resist bending. The external energy E_{ext} drives the contour toward salient edges, and the balloon energy $E_{\text{bal}} = \kappa\, n(s)$ increases the moving distance by embedding a normal force into each snaxel.

A new parameter $j(s)$ is defined as:

$$j(s) = \frac{|\nabla I|_{\max} - |\nabla I(v(s))|}{|\nabla I|_{\max} - |\nabla I|_{\min}}, \tag{10}$$

where $|\nabla I|_{\max}$ and $|\nabla I|_{\min}$ are the maximum and minimum magnitudes of the image gradients, respectively. Consequently, snaxels associated with high gradient values will have smaller values of $j(s)$. This $j(s)$ is further used to adjust the balance between κ and $\beta(s)$ by modifying the energy functions as:

$$E_{\text{int}}(v(s)) = \alpha|v_s|^2 + j(s)^{-1}\beta|v_{ss}|^2, \tag{11}$$

and

$$E_{\text{bal}} = j(s)\kappa n(s). \tag{12}$$

Doing this, snaxels associated with a large value of $j(s)$ will have a relatively smaller value of $j(s)^{-1}\beta$, but a relatively larger value of $j(s)\kappa$. Smaller values of $j(s)^{-1}\beta$ will strengthen the elasticity while larger values of $j(s)\kappa$ will increase the balloon force, leading to more robust segmentation.

2.3 MR image data

We evaluated the proposed algorithm using the internet brain segmentation repository (IBSR) data set in which brain MR images along with their ground truth segmentation results were provided by the Center for Morphometric Analysis (CMA) at Massachusetts General Hospital [19]. The IBSR is a public Wide Web resource providing access to MR brain image data and segmentation results, which is supported by the NIH under Grant number 1 R01 NS34189-01 from the National Institute of Neurological Disorders and Stroke (NINDS). The T1-weighted coronal scans from people with different ages are positionally normalized in each volume. The first data set we obtained in IBSR contains 10 subjects, each of which consists of 128 slices. The dimension of each slice in this IBSR10 image data is 256 × 256 pixels. The second data set was obtained from 20 young middle aged individuals, which we referred to as IBSR20. Each subject includes 60 to 65 slices, and each slice is 3.1 mm thick with a dimension of 256 × 256 pixels. These two image data sets are real scans and suffer from inhomogenities and noise in some slices. Additionally, volumes in the IBSR20 data set contain a large area of the neck and shoulder that could severely bias the performance. For fair competition, regions contain the neck and shoulder were manually removed beforehand.

Simulated brain MR image volumes obtained from the McGill Brain Web [18] were also used to evaluate our method. The images were generated from the normal brain database using the T1 modality, 3 mm slice thickness with various combinations of 1, 3, 5, 7, and 9 % noise levels along with 0, 20, and 40 % intensity nonuniformity settings that produced 15 different subjects, which is referred to as SBD15.

2.4 Performance evaluation metrics

To provide quantitative evaluation of skull-stripping methods, we compute different similarity indexes between the segmentation result R_1 and the ground truth (gold standard) mask R_2. The overlapping area is expected to be as larger as possible, which can be evaluated using the true-positive (θ_{TP}) index. On the other hand, the false-negative (θ_{FN}) index is the nonsegmented region that should be included in actual. It is clear that $R_1 = \{\theta_{\text{TP}} \cup \theta_{\text{FP}}\}$ and $R_2 = \{\theta_{\text{TP}} \cup \theta_{\text{FN}}\}$. More specifically, conformity κ_c is used to evaluate unity subtracted by the ratio of the amount of the mis-segmented pixels to the amount of correctly segmented pixels using [4]

$$\kappa_c \equiv \left(1 - \frac{\theta_{\mathrm{FP}} + \theta_{\mathrm{FN}}}{\theta_{\mathrm{TP}}}\right). \quad (13)$$

It has been shown that conformity is more sensitive and precise than existing measurement coefficients such as Jaccard and Dice in detecting small variations in segmented images.

Alternatively, sensibility η_{sbl} and sensitivity η_{stv} aim to evaluate local segmentation performance. Sensibility locally characterizes how many pixels outside the ground truth are segmented and excludes the impact of image background properties, thus providing consistent evaluation scores [4]:

$$\eta_{\mathrm{sbl}} \equiv \left(1 - \frac{\theta_{\mathrm{FP}}}{\theta_{\mathrm{TP}} + \theta_{\mathrm{FN}}}\right). \quad (14)$$

Contrarily, sensitivity measures the number of pixels located in the ground truth R_2, which is correctly segmented, without considering other regions outside R_2 [11]:

$$\eta_{\mathrm{stv}} \equiv \left(\frac{\theta_{\mathrm{TP}}}{\theta_{\mathrm{TP}} + \theta_{\mathrm{FN}}}\right). \quad (15)$$

One more evaluation metric is the false-positive rate φ_{fpr}, which measures the over-segmentation level and is calculated as the rate of the incorrectly segmented region divided by the ground truth [6]:

$$\varphi_{\mathrm{fpr}} \equiv \left(\frac{\theta_{\mathrm{FP}}}{\theta_{\mathrm{TP}} + \theta_{\mathrm{FN}}}\right). \quad (16)$$

3 Results

All experiments were performed on a Core i3-380M 2.83 GHz machine with 4 GB of main memory running Microsoft Windows 7. The proposed algorithm was implemented using Matlab in which the FPCM toolbox was established from Yashil [42] and the adaptive balloon snake model is modified and extended from the traditional snake model written by Kumar [25]. The experiments were performed to compare our ABS algorithm with other available state-of-the-art methods of LSL [29], BSE [27], WSS [12], and BET [30].

Table 2 presents the performance comparison of the LSL, BSE, WSS, BET, and ABS methods on the IBSR10 data set using different evaluation coefficients. Our ABS algorithm has a better overall performance with more consistent scores of conformity than the LSL, BSE, WSS, and BET methods in skull-stripping these ten subjects. While the sensibility and sensitivity scores of the proposed method are closely high, the scores of other methods are somewhat distinctive and incomparable. To better understand the performance on each individual subject of IBSR10, we present the corresponding scores of conformity, sensibility, and sensitivity in Fig. 5. For the ABS method, it is obvious that the scores of sensibility are pretty high approximately between 0.95 and 1.00 in all subjects, which is also the case for sensitivity in the first six subjects. However, the sensitivity scores drop below 0.95 in the last

Table 2 Performance comparison of LSL, BSE, WSS, BET, and ABS on IBSR10, IBSR20, and SBD15 data sets

	Performance metrics (Avg. ± Std.)			
	κ_c	η_{sbl}	η_{stv}	φ_{fpr}
IBSR10				
LSL	0.8316 ± 0.0364	0.8333 ± 0.0375	0.9985 ± 0.0013	0.1667 ± 0.0375
BSE	0.9022 ± 0.0388	0.9248 ± 0.0371	0.9795 ± 0.0109	0.0752 ± 0.0371
WSS	0.8131 ± 0.2187	0.8235 ± 0.2254	0.9903 ± 0.0130	0.1765 ± 0.2254
BET	0.8519 ± 0.0700	0.8876 ± 0.0430	0.9704 ± 0.0351	0.1124 ± 0.0430
ABS	0.9368 ± 0.0289	0.9777 ± 0.0173	0.9623 ± 0.0340	0.0223 ± 0.0173
IBSR20				
LSL	0.7728 ± 0.1856	0.7808 ± 0.1808	0.9938 ± 0.0092	0.2192 ± 0.1808
BSE	0.8802 ± 0.0493	0.9353 ± 0.0227	0.9526 ± 0.0485	0.0647 ± 0.0227
WSS	0.8346 ± 0.2086	0.8497 ± 0.1826	0.9893 ± 0.0164	0.1503 ± 0.1826
BET	0.6945 ± 0.0587	0.6954 ± 0.0587	0.9993 ± 0.0006	0.3046 ± 0.0587
ABS	0.9083 ± 0.0431	0.9321 ± 0.0322	0.9787 ± 0.0211	0.0679 ± 0.0322
SBD15				
LSL	0.6904 ± 0.0632	0.9060 ± 0.0106	0.8374 ± 0.0466	0.0940 ± 0.0106
BSE	0.8506 ± 0.0185	0.9934 ± 0.0021	0.8760 ± 0.0154	0.0066 ± 0.0021
WSS	0.8763 ± 0.0138	0.9109 ± 0.0210	0.9691 ± 0.0093	0.0891 ± 0.0210
BET	0.9171 ± 0.0078	0.9864 ± 0.0013	0.9360 ± 0.0077	0.0136 ± 0.0013
ABS	0.9425 ± 0.0048	0.9481 ± 0.0052	0.9947 ± 0.0010	0.0519 ± 0.0052

four subjects (same tendency for the BSE and BET methods), which results in poor overall scores of conformity.

The performance of our algorithm on the IBSR20 data set in comparison with the LSL, BSE, WSS, and BET methods is presented in Table 2 based on the conformity, sensibility, sensitivity, and false-positive rate. Once again, the ABS method outperformed other methods in providing higher overall conformity scores. While the LSL, WSS, and BET methods produced pretty high sensitivity scores, their sensibility values were much smaller than other methods. Both BSE and ABS methods provided somewhat consistent scores of sensibility and sensitivity. Note that the false-positive rates of the BET and LSL methods are extremely high comparing to other methods, which dramatically drags the conformity scores below 0.70 and 0.78, respectively. Table 2 also summarizes the performance evaluation scores of the five methods on the SBD15 data set. Our algorithm achieved a higher average score of conformity (0.9425) with less standard deviation comparing with other methods.

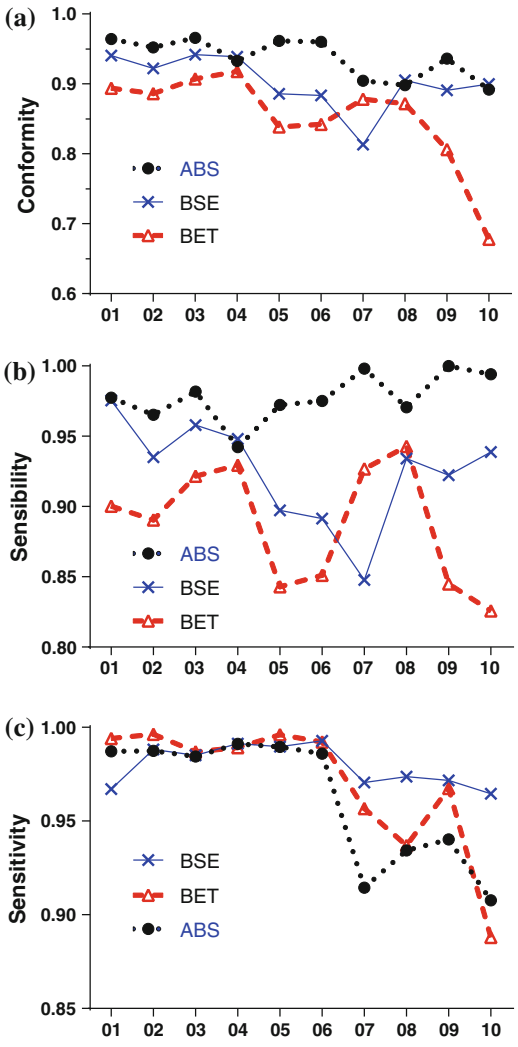

Fig. 5 Comparison of performance evaluation metrics between the BSE, BET, and proposed ABS methods on IBSR10 data set. **a** Conformity. **b** Sensibility. **c** Sensitivity

Finally, we demonstrate qualitative analysis of using our algorithm on some arbitrary selected image volumes. Fig. 6a illustrates visual representations of skull-stripping results along with snake contour evolutions on some slices of the second volume in the IBSR10 data set. Every row represents the same slice with different image and processing information. In each individual row, the original image I is shown in the first column, and the enhanced image I_{enh} associated with the initial contour (the yellow curve) is shown in the second column. In the third column, we show the final contour associated with the final segmentation result. For reference, the corresponding ground truth is shown in the last column. Other examples of subject 4_8 in the IBSR20 data set are illustrated in Fig. 6b. In both illustrations, it is clear that all initial snake contours were correctly placed outside the brain after the FPCM procedure and the final evolved contours precisely encompassed the brain surface.

4 Discussion

We have introduced a hybrid methodology for skull-stripping brain MR images based on an adaptive balloon snake model. Generally, the brain is surrounded by the CSF, whose intensity is lower than the adjacent skull and GM in T1-weighted MR images. However, there may exist some strong linkages between these tissues that cause ambiguous patches and blurred boundaries. To deal with this difficulty, the FPCM algorithm is first applied to partition the brain into five clusters, one of which representing the CSF is further enhanced to facilitate contour initialization.

Most existing contour based skull-stripping methods initialize the contour inside the brain region based on intensity thresholding and histogram analysis. The initial contour could be conservatively placed within the brain region while it suffers from noise sensitivity problems owing to a relatively longer moving distance. Inspired by such limitation and Segonne's work [26], our algorithm initializes the contour just outside the brain region. Comparatively, unwanted noise effect is relieved using this strategy, which has the advantages of short moving distance, automation without user intervention and high accuracy.

In practice, the coefficients α, β, and κ in the balloon snake model are generally set to constants in many applications for simplicity. This may have satisfactory performance in segmenting objects with simple geometries and clear boundaries. However, the complex anatomical structure and unexpectable intensity variation in brain MR

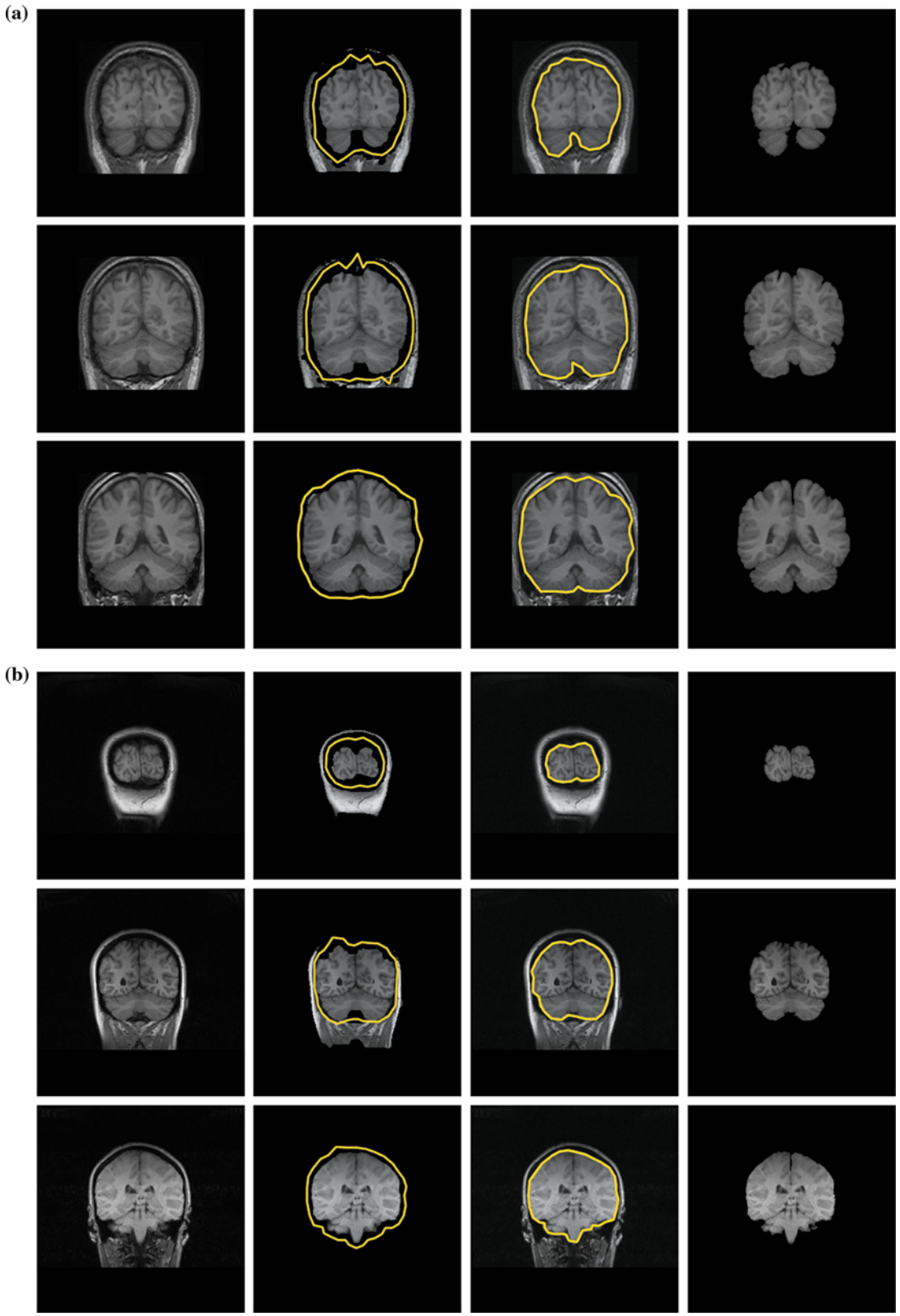

Fig. 6 Qualitative illustration of skull-stripping results using the ABS algorithm. *First column*: original images, *second column*: enhanced images with initial contours, *third column*: final contours, and *last column*: ground truths. **a** Subject 02 of the IBSR10 data set. *First row*: slice 20, *second row*: slice 30, and *third row*: slice 40. **b** Subject 4_8 of the IBSR20 data set. *First row*: slice 5, *second row*: slice 15, and *third row*: slice 23

images make it a challenging task. To address this problem, we proposed an enhanced model with an adaptive weighting function incorporating into the traditional snake contour, which is driven by the guidance of this new integrated balloon force. The design is based on the assumption that snaxels are associated with high image gradients when they locate at the target boundary. Contrarily, snaxels accompany lower gradients when they locate at homogeneous regions.

Since the proposed method placed the initial contour outside the brain and shrank to capture the brain boundary, the segmented region was always smaller than the initial contour, which maintained high and consistent scores of sensibility in all subjects as can be realized in Table 2. The robustness of our algorithm across various noise levels and intensity nonuniformity settings was validated by the high performance evaluation scores of the SBD15 data set. The inconsistent performance of sensitivity of the IBSR10 data set shown in Fig. 5c is probably because that the topological boundaries of the brain are relatively smoother in the preceding six subjects while the brain contains several convexities and concavities in the last four subjects. These convexities and concavities trapped initially estimated snaxels on several slices, leading to difficult contour advancement.

In addition, most evaluated skull-stripping techniques had poor performance with lower conformity scores on the IBSR20 data set comparing to the IBSR10 data set. The degree of degradation is somewhat slight for the LSL, BSE, and ABS methods, but severe for the BET method. This is partially resulted from the double amounts of image data and more significant artifact of inhomogeneity in the IBSR20 data set. The higher score of the false-positive rate in the BET method indicates the inherited over-segmentation problem. This problem is due to the fact that the snake contour in the BET method is initialized inside the brain and evolved outward to capture the brain boundary. In situations of severely blurred brain boundaries, no strong image forces are presented to stop the contour, leading to leakage. On the other hand, the snake contour of our algorithm is advancing inward and stopped at the brain surface that provides more accurate results.

One limitation of the ABS algorithm is the splitting of contours for multi-object segmentation, which also exists in many snake models. In the axial (transversal) view of brain MR images, the brain is separated into two lobes on several lower-end slices. Currently, the proposed method segmented these separated lobes using one entire contour, which can deteriorate the performance. Nevertheless, these regions are somewhat small, and the influence is quite slight comparing to contour leakage. Topological changes based on snake models are usually complicated, time consuming, and difficult to implement. Contrarily, the evolution of the proposed balloon snake model is time efficient and easy to implement. Regardless, the investigation of introducing splitting and merging abilities into the ABS model will be interesting, but challenging in the future.

Lastly, the balloon snake contour in the proposed ABS framework is evolved by the adaptive balloon force in one single inward direction with the snaxels initialized outside the brain surface. One possible way for future research is to locate the contour around the brain boundary and adopt bidirectional evolution, which deflates and inflates the contour simultaneously. With this bidirectional deformation force, the ABS algorithm may provide more flexibility and achieve better performance. The accuracy of our method extensively depends on the precision of contour initialization associated with the FPCM result. In MR images, the slices around both ends somewhat suffer from non uniformity and shading effects, which more or less mislead our FPCM clustering. To investigate the use of machine learning techniques such as the SVM and to incorporate artifact rectification, techniques in the image preprocessing step will be beneficial to more robust segmentation.

In summary, we proposed a new hybrid skull-stripping algorithm based on an adaptive snake model associated with a FPCM cluster. The proposed method was validated using a wide variety of brain MR image volumes in various data sets. Experimental results indicated that our algorithm outperformed several state-of-the-art methods in achieving more accurate skull-stripping results. While further research is advantageous to achieve better performance, we believe that our ABS technique is efficient and promising in a variety of brain image segmentation applications.

Acknowledgements This work was supported in part by the Center for Advanced Theoretical Sciences and National Science Council under Research Grant No. NSC100-2320-B-002-073-MY3.

Appendix 1: Cluster analysis

Cluster analysis aims to partition a set of objects into several groups (clusters) by assigning different labels to each individual object. In general, groups are identified according to some specific senses such as connectivity-based, distribution-based, and centroid-based classification. A clustering algorithm can be generally defined as clustering an unlabeled data set $D = \{d_1, d_2, \ldots, d_n\}$ into c subgroups, where $1 < c < n$ is the number of the clusters usually predefined by the user. Vectors in the same partition are assigned with an identical label. The c-partition of D can be arrayed as a matrix $U_{c \times n} = [u_{ik}]$ with size

$c \times n$. The value of u_{ik} varies between different clustering algorithms. Moreover, a set of centroids or prototypes $V = \{v_1, v_2, \ldots, v_c\}$ is further defined for representing each cluster in centroid-based models.

The fuzzy c-means (FCM), proposed by Bezdek [2], is a centroid-based model that incorporates the fuzzy concept in the membership, i.e., the membership of each object d_k is defined as the inversely relative distance of d_k to the centroid V. The membership of the data set can be arrayed as $U_{\mathrm{FCM}} = [u_{ik}]$ and is constrained by the following equations:

$$\sum_{i=1}^{c} u_{ik} = 1, \quad \forall k \tag{17}$$

and

$$\sum_{k=1}^{n} u_{ik} > 0, \quad \forall i. \tag{18}$$

Equation (17) indicates that the membership of an object d_k in each cluster is a normalized value such that the membership of d_k sums to 1 while Eq. (18) implies that there exists at least one object associated with positive membership in each centroid.

Since the membership is the inverse function of the object distance to the centroid, one problem of the FCM is that for points that are naturally identified as outliers but equidistant from two prototypes, the same membership is given to these points. The calculated values of membership thus provide unrepresentative associations between objects and prototypes. Such drawback is resulted from Eq. (17) in that the membership is normalized and unable to present the actual spatial relationship.

Subsequently, Krishnapuram and Keller [15] proposed the possibilistic c-means (PCM), in an attempt to relieve the problem in the FCM. The PCM model replaces the column sum constraint with a looser form as:

$$0 < \sum_{i=1}^{c} u_{ik} < c \quad \forall k \, \exists i \ni u_{ik} > 0, \tag{19}$$

where each element u_{ik} is between 0 and 1. The value of u_{ik} is interpreted as typicality instead of membership of d_k relative to the centroid v_i. It is also recommended to interpret each row of U as a possibility distribution over D. The PCM model somewhat overcomes the drawbacks of the FCM while it sometimes suffers from coincident cluster problems, which refer to incorrect assignment of an object that naturally belongs to another [1].

Fuzzy possibilistic c-means (FPCM), as the name implies, combines the features of the fuzzy and possibilistic c-means and address the problems of these two models. The FPCM finds out the optimal solution of classification by minimizing the following objective function,

$$\min_{\mathbf{U},\mathbf{T},\mathbf{V}} J_{m,\eta}(\mathbf{U},\mathbf{T},\mathbf{V};\mathbf{X}) = \sum_{i=1}^{c}\sum_{k=1}^{n}(u_{ik}^{m} + t_{ik}^{\eta})||x_k - v_i||^2, \tag{20}$$

where $\mathbf{U}$ denotes the relative typicality (membership) described in the FCM, $\mathbf{T}$ represents the absolute typicality in the PCM, and $\mathbf{V}$ is a vector of element v_i representing the center belonging to cluster i. The symbols m and η are weighting exponents with $m > 1$ and $\eta > 1$. The constant c is the number of clusters and k the number of data points. Details of the minimization process and proof are given in [20]. Herein, we briefly describe the necessary conditions for minimizing the objective function $J_{m,\eta}$ as follows:

$$u_{ik} = \left[\sum_{j=1}^{c}\left(\frac{||x_k - v_i||}{||x_k - v_j||}\right)^{\frac{2}{m-2}}\right]^{-1}, \quad \forall i, k \tag{21}$$

and

$$t_{ik} = \left[\sum_{j=1}^{n}\left(\frac{||x_k - v_i||}{||x_j - v_i||}\right)^{\frac{2}{\eta-2}}\right]^{-1}, \quad \forall i, k. \tag{22}$$

Based on these conditions, vector $\mathbf{V}$ is updated using

$$v_i = \frac{\sum_{k=1}^{n}(u_{ik}^{m} + t_{ik}^{\eta})x_k}{\sum_{k=1}^{n}(u_{ik}^{m} + t_{ik}^{\eta})}, \quad \forall i. \tag{23}$$

Appendix 2: Balloon snake models

Snakes (also known as parametric active contours), proposed by Kass et al. [14], have been widely applied in image segmentation and object tracking. A snake can be defined as a set of ordered points or snaxels $v(s) = [x(s), y(s)]$, usually generated counter-clockwise. The parameter $s \in [0, 1]$ is a normalized arc length starting from the first snaxel. The deformation of each snaxel is governed by both internal and external forces. The internal force is related to the stretching ability (or tension) and smoothness of the curve, which shrinks to a tiny circle when the driving forces are only internal. While the internal force is independent from the image data, the external force is related to salient features such as terminations and edges in images. The balance of internal and external forces drives the snake curve moving toward the object boundary while simultaneously maintaining the tension and stiffness.

Subsequently, Cohen et al. [8] embedded a balloon force into the traditional snake models to solve the problem of limited moving distances. This enhanced version of snakes simulates the action of balloons including deflation and inflation along the normal direction. An overview of the balloon snake model is shown in the following equation:

$$E_{\text{snake}} = \int_0^1 E_{\text{int}}(v(s)) + E_{\text{ext}}(v(s)) + E_{\text{bal}}(v(s))\text{d}s, \quad (24)$$

where E_{int}, E_{ext} and E_{bal} represent the internal, external, and balloon energy, respectively.

The internal energy in Eq. (24) is defined as:

$$E_{\text{int}} = \alpha(s)|v_s|^2 + \beta(s)|v_{ss}|^2, \quad (25)$$

where $\alpha(s)$ and $\beta(s)$ are weighting functions, and subscripts are used to indicate derivatives. The first order derivative with respect to s controls the distance between adjacent snaxels. During energy minimization, the second order term makes the contour resist bending. Consequently, the snake contour tends to collapse in the absence of other constraints or forces. The relative strength of tension and stiffness can be adjusted by controlling the values of $\alpha(s)$ and $\beta(s)$.

Alternatively, the external energy in Eq. (24) is defined as

$$E_{\text{ext}} = -\gamma \mid \nabla G_\sigma(x,y) \times I(x,y) \mid^2, \quad (26)$$

where G_σ denotes the Gaussian filter with σ controlling the spatial extent of the local minima of the convolution kernel, ∇ is the gradient operator, I is the image intensity, and the notation $|\cdot|$ represents norm. The parameter γ is a weighting function for controlling the magnitude of the external energy. Accordingly, regions with salient features have relatively smaller external energy while homogeneous regions are associated with higher external energy.

By embedding a normal force into each snaxel, the balloon energy increases the moving distance using:

$$E_{\text{bal}} = \kappa n(s). \quad (27)$$

where κ is a weighting function and $n(s)$ is the normal vector that is further resolved into x and y components:

$$n_x(s) = \frac{y_{s+1} - y_{s-1}}{\sqrt{(x_{s+1} - x_{s-1})^2 + (y_{s+1} - y_{s-1})^2}} \quad (28)$$

and

$$n_y(s) = \frac{-(x_{s+1} - x_{s-1})}{\sqrt{(x_{s+1} - x_{s-1})^2 + (y_{s+1} - y_{s-1})^2}} \quad (29)$$

where x_s and y_s in pair represent the coordinates of the sth snaxel.

According to the theory of the fundamental Euler-Lagrange differential equation and minimizing E_{snake}, the snake evolution is achieved when the following equation is satisfied:

$$F_{\text{int}} + F_{\text{ext}} + F_{\text{bal}} = 0 \quad (30)$$

where

$$F_{\text{int}} = \alpha(s)v_{ss} - \beta(s)v_{ssss}, \quad (31)$$

$$F_{\text{ext}} = -\nabla E_{\text{ext}}, \quad (32)$$

and

$$F_{\text{bal}} = \nabla E_{\text{bal}}. \quad (33)$$

References

1. Barni M, Cappellini V, Mecocci A (1996) Comments on a possibilistic approach to clustering. Fuzzy Syst IEEE Trans 4(3):393–396. doi:10.1109/91.531780
2. Bezdek JC (1981) Pattern recognition with fuzzy objective function algorithms. Kluwer Academic Publishers, Norwell, MA, USA
3. Boesen K, Rehm K, Schaper K, Stoltzner S, Woods R, Lders E, Rottenberg D (2004) Quantitative comparison of four brain extraction algorithms. NeuroImage 22(3):1255–1261
4. Chang HH, Zhuang AH, Valentino DJ, Chu WC (2009) Performance measure characterization for evaluating neuroimage segmentation algorithms. NeuroImage 47(1):122–135. doi:10.1016/j.neuroimage.2009.03.068
5. Charfi M (2010) Using the ggvf for automatic initialization and splitting snake model. In: I/V communications and mobile network (ISVC), 5th international symposium on IEEE. pp 1–4. doi:10.1109/ISVC.2010.5656426
6. Chiverton J, Wells K, Lewis E, Chen C, Podda B, Johnson D (2007) Statistical morphological skull stripping of adult and infant mri data. Comput Biol Med 37(3):342–357. doi:10.1016/j.compbiomed.2006.04.001
7. Cohen L, Cohen I (1993) Finite-element methods for active contour models and balloons for 2-d and 3-d images. Pattern Anal Mach Intell IEEE Trans 15(11):1131–1147. doi:10.1109/34.244675
8. Cohen LD (1991) On active contour models and balloons. CVGIP Image Underst 53:211–218. doi:10.1016/1049-9660(91)90028-N
9. Ellis CA, Parbery SA (2005) Is smarter better? a comparison of adaptive, and simple moving average trading strategies. Res Int Bus Financ 19(3):399–411. doi:10.1016/j.ribaf.2004.12.009
10. Fennema-Notestine C, Ozyurt IB, Clark CP, Morris S, Bischoff-Grethe A, Bondi MW, Jernigan TL, Fischl B, Segonne F, Shattuck DW, Leahy RM, Rex DE, Toga AW, Zou KH, Brown GG (2006) Quantitative evaluation of automated skull-stripping methods applied to contemporary and legacy images: effects of diagnosis, bias correction, and slice location. Hum Brain Mapp 27(2):99–113
11. Fenster A, Chiu B (2005) Evaluation of segmentation algorithms for medical imaging. In: Engineering in Medicine and Biology Society. IEEE-EMBS 2005. 27th annual international conference. pp 7186–7189. doi:10.1109/IEMBS.2005.1616166
12. IDeA (2013) IDeA lab: imaging of dementia and aging, Center for Neuroscience, UC Davis. http://idealab.ucdavis.edu/
13. Ji Y, Sun S (2013) Multitask multiclass support vector machines: model and experiments. Pattern Recognit 46(3):914–924
14. Kass M, Witkin A, Terzopoulos D (1988) Snakes: active contour models. Int J Comput Vis 1(4):321–331
15. Krishnapuram R, Keller J (1993) A possibilistic approach to clustering. Fuzzy Syst IEEE Trans 1(2):98–110. doi:10.1109/91.227387

16. Li CM, Liu JD, Fox M (2005) Segmentation of edge preserving gradient vector flow: an approach toward automatically initializing and splitting of snakes. In: Computer vision and pattern recognition. CVPR 2005. IEEE computer society conference, vol 1. pp 162–167. doi:10.1109/CVPR.2005.314
17. Li H, Yezzi A, Cohen LD (2006) 3d brain segmentation using dual-front active contours with optional user interaction. Int J Biomed Imaging (Article ID 53186):17. doi:10.1155/IJBI/2006/53186
18. McGill (2011) BrainWeb: simulated brain database. http://www.bic.mni.mcgill.ca/brainweb/
19. MGH (2003) Internet brain segmentation repository (IBSR). http://www.cma.mgh.harvard.edu/ibsr/, Accessed 06 Dec 2003
20. Pal N, Pal K, Bezdek J (1997) A mixed c-means clustering model. In: Fuzzy systems. Proceedings of the sixth IEEE international conference, vol 1. pp 11–21. doi:10.1109/FUZZY.1997.616338
21. Pal N, Pal K, Keller J, Bezdek J (2005) A possibilistic fuzzy c-means clustering algorithm. Fuzzy Syst IEEE Trans 13(4):517–530. doi:10.1109/TFUZZ.2004.840099
22. Park JG, Lee C (2009) Skull stripping based on region growing for magnetic resonance brain images. NeuroImage 47(4):1394–1407. doi:10.1016/j.neuroimage.2009.04.047
23. Phumeechanya S, Pluempitiwiriyawej C, Thongvigitmanee S (2010) Edge type-selectable active contour using local regional information on extendable search lines. In: Image processing (ICIP), 17th IEEE international conference. pp 653–656. doi:10.1109/ICIP.2010.5650160
24. Pitiot A, Delingette H, Thompson PM, Ayache N (2004) Expert knowledge-guided segmentation system for brain {MRI}. NeuroImage 23(Suppl 1):S85–S96. doi:10.1016/j.neuroimage.2004.07.040
25. Rkkumar (2011) Snakes—Active contour models: demonstrates the use active contour models. http://www.seas.harvard.edu/~rkkumar. Accessed 01 Aug 2011
26. Sgonne F, Dale A, Busa E, Glessner M, Salat D, Hahn H, Fischl B (2004) A hybrid approach to the skull stripping problem in MRI. NeuroImage 22(3):1060–1075. doi:10.1016/j.neuroimage.2004.03.032
27. Shattuck DW, Sandor-Leahy SR, Schaper KA, Rottenberg DA, Leahy RM (2001) Magnetic resonance image tissue classification using a partial volume model. NeuroImage 13(5):856–876. doi:10.1006/nimg.2000.0730
28. Shawe-Taylor J, Sun S (2011) A review of optimization methodologies in support vector machines. Neurocomputing 74(17):3609–3618. doi:10.1016/j.neucom.2011.06.026
29. Shi F, Wang L, Dai Y, Gilmore JH, Lin W, Shen D (2012) Label: pediatric brain extraction using learning-based meta-algorithm. NeuroImage 62(3):1975–1986. doi:10.1016/j.neuroimage.2012.05.042
30. Smith SM (2002) Fast robust automated brain extraction. Hum Brain Mapp 17(3):143–155. doi:10.1002/hbm.10062
31. Stokking R, Vincken KL, Viergever MA (2000) Automatic morphology-based brain segmentation (mbrase) from mri-t1 data. NeuroImage 12(6):726–738. doi:10.1006/nimg.2000.0661
32. Sun S, Zhang C (2006) Adaptive feature extraction for eeg signal classification. Med Biol Eng Comput 44(10):931–935. doi:10.1007/s11517-006-0107-4
33. Suri JS, Farag AA, Micheli-Tzanakou E, Das B, Banerjee S (2007) Parametric contour model in medical image segmentation. In: Deformable models, topics in biomedical engineering. International Book Series, Springer New York, pp 31–74
34. Tanoori B, Azimifar Z, Shakibafar A, Katebi S (2011) Brain volumetry: An active contour model-based segmentation followed by svm-based classification. Comput Biol Med 41(8):619–632. doi:10.1016/j.compbiomed.2011.05.013
35. Tao XD, Chang MC (2010) A skull stripping method using deformable surface and tissue classification. In: Proceedings on SPIE medical imaging, vol 7623. doi:10.1117/12.844061
36. Tomasi C, Manduchi R (1998) Bilateral filtering for gray and color images. In: Computer Vision. Sixth international conference IEEE. pp 839–846. doi:10.1109/ICCV.1998.710815
37. Tong CS, Yuen PC, Wong YY (2002) Dividing snake algorithm for multiple object segmentation. Opt Eng 41:3177–3182. doi:10.1117/1.1517289
38. Wang L, Li C, Sun Q, Xia D, Kao CY (2009) Active contours driven by local and global intensity fitting energy with application to brain {MR} image segmentation. Comput Med Imaging Graph 33(7):520–531. doi:10.1016/j.compmedimag.2009.04.010
39. Wang YH, Fu YL (2011) Research on segmentation methods of brain using mri images. In: 2011 international conference on energy and environmental science—ICEES 2011, IEEE, 11:2382–2388. doi:10.1016/j.egypro.2011.10.555
40. Wang YQ, Liu LX, Zhang H, Cao ZL, Lu SP (2010) Image segmentation using active contours with normally biased gvf external force. Signal Process Lett IEEE 17(10):875–878. doi:10.1109/LSP.2010.2060482
41. Xu CY, Prince J (1997) Gradient vector flow: a new external force for snakes. In: Computer Vision and Pattern Recognition. Proceedings on IEEE computer society conference. pp 66–71. doi:10.1109/CVPR.1997.609299
42. Yashil (2010) Fuzzy c-means clustering MATLAB toolbox. http://yashil.20m.com/. Accessed 28 Nov 2010